

MULTI-VARIABLE PHASE AND GAIN CALIBRATION FOR MULTI-CHANNEL TRANSMIT SIGNALS

A thesis submitted in partial fulfillment
of the requirements for the degree of
Master of Science in Electrical Engineering

by

RYAN C. BALL
B.S.E.E., Wright State University, 2021

2023
Wright State University

Wright State University
College of Graduate Programs and Honors Studies

April 21, 2023

I HEREBY RECOMMEND THAT THE THESIS PREPARED UNDER MY SUPERVISION BY Ryan C. Ball ENTITLED Multi-Variable Phase and Gain Calibration for Multi-Channel Transmit Signals BE ACCEPTED IN PARTIAL FULFILLMENT OF THE REQUIREMENTS FOR THE DEGREE OF Master of Science in Electrical Engineering.

Michael A. Saville , Ph.D., P.E.
Thesis Director

Michael A. Saville, Ph.D., P.E.
Chair, Department of Electrical Engineering

Committee on
Final Examination

Michael A. Saville, Ph.D., P.E.

Josh Ash, Ph.D.

Zhiqiang Wu, Ph.D.

Shu Schiller, Ph.D.
Interim Dean, College of
Graduate Programs & Honors Studies

ABSTRACT

Ball, Ryan C. M.S.E.E., Department of Electrical Engineering, Wright State University, 2023.
Multi-Variable Phase and Gain Calibration for Multi-Channel Transmit Signals.

A method for software-defined radio array calibration is presented. The method implements a matched filter approach to calculate the phase shift between channels. The temporal stability of the system and calibration coefficients are shown through the standard deviation over the course of four weeks. The standard deviation of the phase correction was shown to be less than 2° for most channels in the array and within 8° for the most extreme case. The standard deviation in amplitude scaling was calculated to be less than 0.06 for all channels in the array. The performance of the calibration is evaluated by the antenna gain and the difference from the ideal beam shape for the peak side lobe level and first null depth. For one example data collection, the gain was 61 dB for the array with a maximum difference of 0.2246 dB for the peak side lobe level and 0.3998 dB for the first null depth.

Contents

1	Introduction	1
1.1	Software Defined Radio Arrays	1
1.2	Challenges with SDR Arrays	2
1.3	Research Hypothesis	3
1.4	Thesis Outline	3
2	Background	4
2.1	Calibration Methods	4
2.1.1	Calibrating Mutual Coupling	5
2.1.2	Calibration of a SDR Uniform Linear Array	7
2.1.3	Continuous Waveform Calibration	9
2.1.4	Pilot Signal Based Calibration	10
3	Methodology	13
3.1	Introduction	13
3.2	Signal Model	13
3.3	System Model	14
3.4	Matched Filter Calibration	16
3.5	Analysis Methods	18
3.5.1	Temporal Analysis	18
3.5.2	Digital Beamforming Analysis	18
4	Results	21
4.1	Introduction	21
4.2	Data	21
4.3	Phase and Amplitude Error	23
4.3.1	Phase Error	23
4.3.2	Amplitude Error	24
4.4	Phase and Amplitude Correction	25
4.4.1	Phase Correction	25
4.4.2	Amplitude Correction	26
4.5	Effects on Beam Quality	27

4.5.1	Gain	28
4.5.2	First Side Lobe Level	29
4.5.3	First Null	31
4.6	Calibration on Transmit	33
5	Conclusion	43
	Bibliography	45

List of Figures

3.1	SDR system setup in transmit mode	15
3.2	SDR system setup in receive mode	15
3.3	Example of calculated beamforming points for normalized ideal, calibrated, and uncalibrated digital beams	20
4.1	Example of frequency spectrum of channel 1 received chirp at center fre- quency 200 MHz	23
4.2	Channel 1 phase error vs frequency of Feb. 24th received chirp data	24
4.3	Channel 1 amplitude error vs frequency of Feb. 24th received chirp data . .	25
4.4	Phase correction of channel 1 vs frequency for Feb. 24th received chirp data	26
4.5	Standard deviation of phase correction vs channel for center frequencies 200 and 900 MHz	27
4.6	Amplitude correction of channel 1 vs frequency for Feb. 24th received chirp data	28
4.7	Standard deviation of the amplitude correction vs channel for center fre- quencies 200 and 900 MHz	29
4.8	Main lobe gain with different calibrations applied	30
4.9	First side lobe level with different calibrations applied	31
4.10	Calibrated and uncalibrated first side lobe level vs data collect for 200 MHz center frequency	32
4.11	Beamforming results of Feb. 24th data with mean calibration applied for center frequencies 200 and 900 MHz	36
4.12	First null depth with different calibrations applied	37
4.13	Calibrated and uncalibrated first null depth vs data collect for 200 MHz center frequency	38
4.14	Standard deviation of amplitude correction for transmitted chirp signals at 200 and 900 MHz center frequencies	38
4.15	Standard deviation of phase correction for transmitted chirp signals at 200 and 900 MHz center frequencies	39
4.16	Main lobe gain for Mar. 14th data collection calibrated before transmit and recalibrated after receiving	39
4.17	First null depth for Mar. 14th data collection calibrated before transmit and recalibrated after receiving	40

4.18 Peak side lobe level for Mar. 14th data collection calibrated before transmit and recalibrated after receiving 40

4.19 Beamforming results for Mar. 14th data collection calibrated before transmit and recalibrated after receiving 41

4.20 Calibrated Digital Beams for 200 MHz Rx Tone with Different Calibration Methods 42

List of Tables

4.1	Dataset Characteristics	22
4.2	Calculated Gain Values of Rx Tone Data from March 14th Data Collection Calibrated with Different Methods	34
4.3	Calculated Peak Side Lobe Values of Rx Tone Data from March 14th Data Collection Calibrated with Different Methods	34
4.4	Calculated Null Depth Values of Rx Tone Data from March 14th Data Col- lection Calibrated with Different Methods	35

Acknowledgment

I would like to thank Dr. Michael Saville for his guidance, support, and encouragement over the last two years. Your guidance helped my growth as a student and as a researcher. I would also like to thank my committee members Dr. Josh Ash and Dr. Zhiqiang Wu. Thank you to my grandparents Cheryl and Dover Ball for always encouraging me to push through hardships and believing in me. Finally, thank you to Dr. Josh Compaleo for guiding me and being someone I can truly look up to.

This article was cleared for public release on 09 June 2023 (case number: AFRL-2023-2813). The views expressed in this article are those of the authors and do not reflect the official policy or position of the United States Air Force, Department of Defense, or the U.S. Government

Dedicated to
Midnight

Introduction

1.1 Software Defined Radio Arrays

Antenna arrays are widely used in radar and communication systems [1]. They are essential for many systems to be able to achieve their performance objectives. Using antenna arrays provides advantages at the cost of more complex processing of the signals. In array processing, complex-valued weightings are applied to each sensor output to spatially filter the incoming signals. Depending on the weightings applied and the spatial dependence of the incoming signals, signals can be amplified or rejected. The physical position of the array elements are also a factor that can influence the spatial filtering capabilities of an array. The spatial filtering characteristics of an array are typically determined by size constraints.

Along with antenna arrays, software defined radios (SDR) are also widely used in communication systems. The main push for innovation and funding comes from military organizations and groups like NASA [2]. SDRs have lower cost and greater flexibility than radios that are designed for a single signal format [3–6]. SDRs allow transmit, receive, modulation/demodulation, timing, control, coding, and decoding functions to be performed in software [7]. Due to these functions being software controlled, the user has greater flexibility for reconfiguring the signal to an appropriate format. The greater flexibility of SDRs comes with the drawback of higher complexity in calibrating a SDR system.

1.2 Challenges with SDR Arrays

The size of the array manifold often places a constraint on the size of the array. An example of the size constraints are the antenna arrays in modern phones. With small antenna arrays, antenna elements are close to each other, which leads to mutual coupling between elements [8]. Mutual coupling occurs when an antenna couples the transmission from a nearby antenna element. Mutual coupling degrades the signal-to-interference-noise ratio (SINR) and the performance of array processing algorithms. Thus, accounting for the effects of mutual coupling on an array is necessary.

Other challenges with antenna arrays are the phase and amplitude errors that occur as the signal goes through the system. To take advantage of the beamforming ability of antenna arrays, precise control of amplitude and phase is necessary. Phase errors can result in increased side lobe levels and decreased main beam gain in a study by Schediwy et al. [9].

The phase and amplitude errors of a system are complicated further when using SDRs. Unlike a conventional multichannel array with fixed transmit and receive signal pathways, the transmit and receive signal pathways of an SDR can be reconfigured with software control [10]. Each path in an SDR will have a different effective path length, making the phase and amplitude errors different for in each band of operation. Therefore, calibration must be re-applied as the radio is reconfigured. Many of the algorithms proposing calibration methods of SDR arrays do not mention how often the systems need to be calibrated. The required time between calibrations of an SDR array have not been reported and remain unknown.

1.3 Research Hypothesis

This research seeks to establish a methodology for determining the effect of signal frequency, mode of operation, and signal type on phase and amplitude errors for a SDR array system. A system consisting of four SDRs with four channels each will be used to collect transmit and receive data over a wide bandwidth. Digital beamforming will be applied before and after calibration to show the effect calibration has on the beam shape. This study also seeks to understand the temporal stability of SDR array calibration. The temporal stability will be analyzed using statistical measures of the calculated phase and amplitude corrections. The stability of the phase and amplitude will be confirmed by using digital beamforming with signals calibrated on transmit.

1.4 Thesis Outline

Chapter 2 will provide a review of mutual coupling and calibration methods used in SDR arrays. Chapter 3 will present the model of the system and methodology of the proposed calibration algorithm. Chapter 4 will show the phase and amplitude errors, the corresponding calibration correction required, and the results of calibration with digital beamforming. Chapter 5 will offer conclusions regarding the effectiveness of the proposed calibration algorithm and give recommendations for future research.

Background

2.1 Calibration Methods

For antenna arrays, phase error can be especially problematic. A study by Schediwy et al. in [9] shows that a difference in time of arrival results in beamforming errors. This time difference can be due to unequal lengths of transmission lines or phase errors introduced by analog components of the system. If the signals are assumed to be narrowband, phase errors can be related to a time delay in [9, eq. (1)]

$$\Delta t = \frac{1}{2\pi} \frac{\Delta\phi}{f}, \quad (2.1)$$

where Δt is the time delay, $\Delta\phi$ is the phase error, and f is the frequency of the incoming signal. One of the measures of array quality used by Schediwy et al. is the sensitivity of the array. As described by Sun [11], the sensitivity of a receiving array is the ability to receive weak signals. While it is generally expressed in terms of minimum detectable signal level, Schediwy et al. uses a percentage in terms of sensitivity lost. They showed the loss of sensitivity as a function of phase error for 4, 16, and 128 element diameter arrays. Schediwy et al. showed with phase errors of 10° or less, the sensitivity of the array degrades by less than 1%. In order to keep the sensitivity of the array within 95% of the ideal case, the average phase error needed to be less than 25° for the system they were simulating.

The time differences caused by manufacturing differences can be measured when the

incoming signal is perpendicular to the reference plane of the array, also known as boresight. For linear and planar arrays, the reference plane and array manifold are the same. The manufacturing differences can be measured in this way because the plane wave will be incident to all elements of the array at the same time. When the signal is received from an angle that is not boresight, angular dependent time delays are observed in the received signals. These angular dependent time delays will impact the performance of signal processing algorithms such as digital beamforming algorithms [12].

2.1.1 Calibrating Mutual Coupling

There are many methods proposed to calibrate mutual coupling [4, 13]. The method proposed by Xiao [13] uses deep learning to compensate for mutual coupling. Mutual coupling is difficult to model and changes for every antenna array. Deep learning is used in this case to compensate for mutual coupling in a general sense.

Mutual coupling compensation was reviewed in [4] with four methods. In this study, mutual coupling between array elements is assumed to be not present. Only one method of compensating mutual coupling will be reviewed. For each of the four methods presented in the paper, the coupled signals are related to the uncoupled signals with the equation [4, eq. (1)]:

$$\mathbf{v} = \mathbf{C}\mathbf{v}_{ideal}, \quad (2.2)$$

where \mathbf{v} represents the coupled signals, \mathbf{C} is the coupling matrix, and \mathbf{v}_{ideal} represents the uncoupled signals. To recover the uncoupled signals, \mathbf{v}_{ideal} is solved as

$$\mathbf{v}_{ideal} = \mathbf{C}^{-1}\mathbf{v}. \quad (2.3)$$

Since the coupling matrix \mathbf{C} is unknown, the uncoupled signals are estimated as

$$\tilde{\mathbf{v}}_{ideal} = \tilde{\mathbf{C}}^{-1}\mathbf{v}, \quad (2.4)$$

where $\tilde{\mathbf{C}}$ is the estimate for the coupling matrix and $\tilde{\mathbf{v}}_{ideal}$ is the recovered uncoupled signals.

One of the methods reviewed in [4] is titled "The Calibration Method". This method requires that voltage vector \mathbf{v} is measured at different directions of arrival. These calibration points form a matrix \mathbf{V} as follows:

$$\mathbf{V} = [\mathbf{v}_1\mathbf{v}_2\dots\mathbf{v}_M], \quad (2.5)$$

where M is the total number of calibration points collected. With knowledge of the direction of arrival for the calibration points, the ideal voltage matrix is formed as:

$$\mathbf{V}_{ideal} = [\mathbf{v}_{ideal1}\mathbf{v}_{ideal2}\dots\mathbf{v}_{idealM}]. \quad (2.6)$$

With an infinite number of calibration points, (2.5) and (2.6) can be related with the equation,

$$\mathbf{V} = \mathbf{C}\mathbf{V}_{ideal}. \quad (2.7)$$

A finite but large number of measurements across the angular domain are required to calculate the exact mutual coupling matrix for all angles. Since collecting that many calibration points is impractical, an estimate for the mutual coupling matrix is used

$$\mathbf{V} = \tilde{\mathbf{C}}\mathbf{V}_{ideal}. \quad (2.8)$$

To estimate the mutual coupling matrix, the least-square solution is commonly used, given

by [4, eq. (14)]

$$\tilde{\mathbf{C}} = \mathbf{V}\mathbf{V}_{ideal}^H(\mathbf{V}_{ideal}\mathbf{V}_{ideal}^H)^{-1}. \quad (2.9)$$

One of the requirements for this method is to have a number of calibration points at least equal to the number of array elements. Although this is the minimum, the actual number of calibration points required to get a sufficient estimate of C is dependent on the complexity of the antenna array. This method is useful because with knowledge of the direction of arrival and sufficient calibration points, a good estimate of the mutual coupling matrix can be found.

2.1.2 Calibration of a SDR Uniform Linear Array

Campo et al. presented a calibration method for a uniform linear array based on software defined radio [5]. The system in this paper has 2 SDR boards with 2 channels each connected to a uniform linear array working at 2.3 GHz. In the transmit mode, a third SDR is connected to a horn antenna that transmits a signal defined using GNU Radio software [14]. The signal is received by the uniform linear array which is steered by the two receiving SDRs. For the receiving mode, the uniform linear array transmits the signal which is received by the horn antenna. The SDRs connected to the uniform linear array are synchronized using an OctoClock [15] that is fed with a GPS signal. The synchronization of the SDRs with GPS ensures that the clock cycles and sample times are synchronized with each other.

The signal of each channel is sampled as in-phase and quadrature (IQ) format. For channel n , the complex sample is

$$s_n = A_n e^{j\phi_n}, \quad (2.10)$$

where $A_n, \phi_n \in \mathcal{R}$ are the known real-valued amplitude and the known real-valued phase of the signal respectively. In their experiment the authors of [5] assume that channel 1 is

the phase reference channel and the desired amplitude for the calibrated signals is 1. To get the calibration values for any channel n , the correction is

$$c_n = \frac{1}{A_n} e^{j(\phi_1 - \phi_n)}. \quad (2.11)$$

The calibration value is applied to the signal as

$$s'_n = s_n c_n = A_n \frac{1}{A_n} e^{j(\phi_n + \phi_1 - \phi_n)} = e^{j\phi_1}, \quad (2.12)$$

where s'_n is the resulting calibrated signal.

In the receive mode, the authors verified the calibration method with direction of arrival (DoA) estimation. The signals are received, then the calibration is applied, and lastly the DoA is estimated using the Bartlett algorithm. The Bartlett algorithm is a power spectra estimation method that can reduce the variance of the estimation with the cost of reduced resolution [16]. The authors showed that with their method, the error in the estimated angle to the mechanical steered angle was less than $\pm 1.5^\circ$ for the $[-50^\circ, 50^\circ]$ angle range.

In the transmit mode, Campo et al. showed the results of calibration as normalized beam patterns. They compared the results of calibration to the results when using dedicated phase shifters for the uniform linear array. To get the steered beam, the uniform linear array was mechanically steered and the power was measured using the horn antenna. They also showed the results of digitally steering the beam within $[-30^\circ, 30^\circ]$ angular range. They showed through their results that the calibration method proposed was effective in DoA estimation in the $[-50^\circ, 50^\circ]$ angular range and beamforming in the $[-30^\circ, 30^\circ]$ range.

This calibration algorithm assumes that the calibration of the array was performed before operation in the transmit and receive modes. In the receive mode, calibration was applied using the technique described in Equation (2.12) before DoA estimation. In the transmit mode, calibration had to be applied manually for each channel and was performed

using an oscilloscope. The advantages of this calibration procedure are that the calibration correction is easily calculated and can be applied directly to the signal. A disadvantage of this procedure is that the calibration must be performed for each mode before operation.

2.1.3 Continuous Waveform Calibration

Gaydos et al. proposed an algorithm for synchronization and calibration of SDRs in an array [3]. The system used four National Instruments (NI) USRP 2922 SDRs operating at 2.45 GHz to transmit and receive signals in a uniform linear array that will be described in Section 3.3 of this work. Gaydos et al. used a NI CDA-2990 octoclock for time and local oscillator (LO) synchronization across the SDRs. Each SDR had a transmit(Tx)/receive(Rx) port and a second Rx port. The Tx/Rx port was connected to an element of the array. A Signal Hound VSG25A signal generator was used to generate the reference signals. The signal was split using a four way power divider into each of the Rx ports of the SDRs. The correction factors were calculated by recording the received signals for 100 ms. Gaydos et al. calculated the correction factor as [3, (eq. 1)]

$$c_i = \frac{1}{N} \sum_{j=0}^{N-1} \frac{X_{0j}}{X_{ij}}, \quad (2.13)$$

where c_i is the correction factor, N is the number of samples, X is the matrix of complex samples received, j represents the sample number, and i denotes the i^{th} element of the array. This calibration algorithm assumes that the samples used to calibrate the coefficient are from continuous wave (CW) signals. This calibration algorithm can be applied using a pulsed system by only using the samples where the sinusoidal pulse is present.

The calibration method was verified by measuring the phase and amplitude with a fifth NI-USRP 2922. The fifth SDR was also connected to the octoclock for time and LO synchronization. To find the amplitude and phase measurement, they connected the

SDR to each array SDR separately and either transmitted or received a CW signal. They showed their results in a polar plot showing the phase and amplitude of each of the SDRs on transmit and receive before and after applying the correction factor. Gaydos et al. did not report any numerical values for the phase offset of each channel in the array before calibration. The phases and amplitudes of each signal were shown on a polar plot before and after calibration. After calibration, the phases of each channel were much closer but they did not report any specific numbers.

The calibration approach proposed by Gaydos et al. provides advantages and disadvantages. The calibration procedure assumes that the signals transmitted or received are CW signals. This constraint removes the ability to transmit or receive wideband signals. An advantage of this is that it provides a method for calibration of systems that do operate with CW signals. One of the disadvantages is the need for an outside reference signal. If the array is in the receive mode, it is assumed that the receiving array has prior knowledge of the transmitted signal and is replicating it through a signal generator as a reference for each of the channels in the array.

2.1.4 Pilot Signal Based Calibration

The matched filter is another calibration approach used in recent studies. Mazurek and Rytel-Andrianik [6] present a matched filter based calibration that uses pilot sequences to estimate phase shifts. Mazurek and Rytel-Andrianik use two RSPduo devices made by SDRplay [10] in a four channel receiving array. In order to perform estimations of phase shifts and time delays, they inject a pilot sequence into the RF signals. These pilot sequences are widely used in digital communications because they have good correlation properties. The good correlation properties of signals imposed with pilot sequences are useful for detecting signals in low signal-to-noise ratio (SNR) environments. In this research, each pilot signal consists of three copies of an m-sequence generated by a characteristic polynomial. For the transmitted signal, the carrier frequency F_c is tuned to the same fre-

quency as the receiving array. The signal is received by each channel of the array and the pilot signals are combined with the signals from the antenna before being sent to the SDRs. The resulting signals are four digital complex baseband signals $x_k(n)$ ($k = 1, \dots, 4$). The received signals are downconverted as

$$x'_k(n) = x_k(n)e^{-j2\pi nF_0/F_s}, \quad (2.14)$$

where F_0 is the center frequency of the pilot signal and F_s is the sampling frequency. The complex baseband signals are then match filtered as

$$y_k(n) = \sum_{m=0}^{L_s-1} h(m)x'_k(n-m), \quad (2.15)$$

where the real-valued impulse response of the filter $h(m)$ is the m-sequence used to generate the pilot sequence and L_s is the resampled length. They showed that when the pilot sequence was injected into the signal, y_k showed three large peaks denoted as $N_{k,s}$ for $s = 1, \dots, 3$. The averaged differences between the peak positions in the signals $y_k(n)$, $y_l(n)$, provide estimates of the time differences of the signals from the different SDRs ($k, l = 1, \dots, 4$)

$$T_{k,l} = \frac{1}{3} \sum_{s=1}^3 [N_{k,s} - N_{l,s}]. \quad (2.16)$$

With this, the phase shifts between the signals can be estimated as:

$$\phi_{k,l} = \arg\left\{\frac{1}{3} \sum_{s=1}^3 y_k(N_{k,s})y_l^*(N_{l,s})\right\} - 2\pi T_{k,l} \frac{F_0}{F_s}, \quad (2.17)$$

where the last term is a correction for the possible time shift (2.16) between the signals that are downconverted with the same frequency and phase reference (2.14).

The calibration method proposed by Mazurek and Rytel-Andrianik requires a very

specific system. Where the calibration methods discussed in Sections 2.1.2 and 2.1.3 could be used for any system with SDR arrays, the procedure presented in [6] requires the input of a pilot signal. Pilot sequences are widely used in wireless communication systems because of their good correlation properties and can be helpful in channel estimation [17–19]. A disadvantage of using pilot sequences is that they require additional equipment to generate them. Mazurek and Rytel-Andrianik used an 8-bit RISC microcontroller to generate the m-sequence that was used to create the pilot signal. Although the pilot signal is unable to be used for the system in this research, the general idea of using a matched filter can be applied to an array as long as the signals being transmitted or received are assumed to be the same for each array element.

Methodology

3.1 Introduction

This chapter outlines the approach to characterize the effect signal frequency, mode of operation, and signal type have on the phase and amplitude errors for a SDR array system. The phase and amplitude errors will be calculated with a matched filter approach that will be described in Section 3.4 of this paper. The approach to verify the temporal stability of the SDR system will be outlined in this chapter as well. Digital beamforming will also be discussed as a method to show the effectiveness of the proposed calibration method.

3.2 Signal Model

For the sampled reference signal with amplitude A , frequency f , sampling interval Δt , and phase offset ϕ_0 , the k -th time-sample is

$$s(k) = Ae^{j(2\pi fk\Delta t + \phi_0)}. \quad (3.1)$$

For an antenna array with M' transmit channels and M receive channels, each transmit-receive pathway has phase and gain errors accrued as the signal goes through the system.

These signals can be represented with the form,

$$s_{m',m}(k) = Ae^{j(2\pi fk\Delta t + \phi_0)} A_{m',m} e^{\phi_{m',m}} \quad (3.2)$$

The subscripts m' and m represent the m' th transmit channel and m th receive channel. Due to hardware specifications, the phase and gain errors are also dependent on the frequency of the signal. In this study, a discrete number of frequency samples are used and annotated as the n -th frequency using a third subscript as

$$s_{m',m,n}(k) = A_{m',m,n} e^{j(2\pi f_n k \Delta t + \phi_{m',m,n})} \quad (3.3)$$

3.3 System Model

The system used in this experiment includes 4 FPGA boards with 4 transmit/receive channels each. All of the boards are synchronized with an external clock to ensure samples are synchronized across the system. In the transmit mode, each of the channels are combined using a power combiner and transmitted to another FPGA board that receives all 16 signals. In Figure 3.1, the system is shown for the transmit mode. For the purpose of this experiment, only one channel transmits at a time so that we can separate the signals from each transmit path. The signal being sent is a complex signal defined by the user. A file containing the digital signal is loaded into GNU Radio and generated by the software-defined-radios on each FPGA board. The signals can be defined differently for each channel but for the purpose of this research, we assume the signal being transmitted is the same for each channel. During the processing of the received signals, we find the calibration matrix required for each transmit channel of the array. In the receive mode, the system is reversed. Figure 3.2 shows the system in the receive mode. One channel trans-

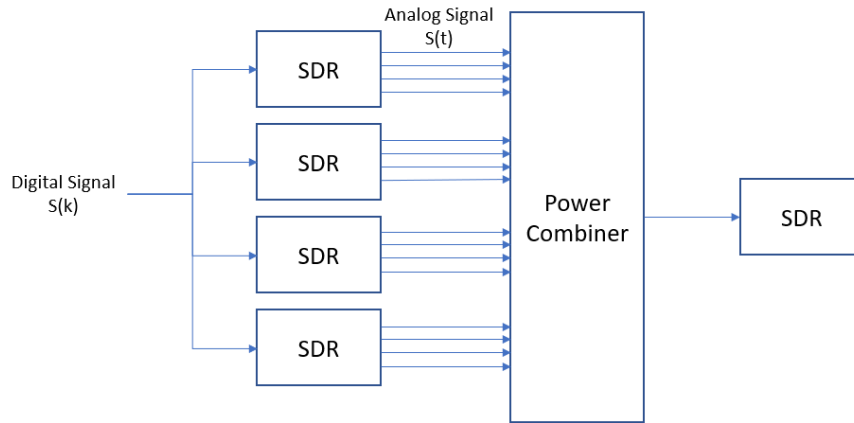


Figure 3.1: SDR system setup in transmit mode

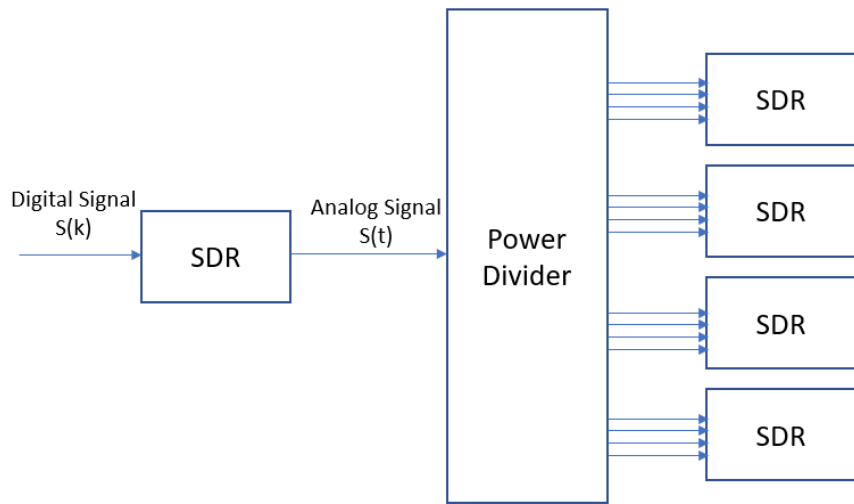


Figure 3.2: SDR system setup in receive mode

mits a signal that is split through a power divider to each of the 16 receiving channels. The signal is defined by the user and generated using the software-defined-radio of the transmitting channel. During processing of the received signal, complex calibration coefficients are calculated for each of the receive channels in the array.

3.4 Matched Filter Calibration

The system used in this research, as described in Section 3.3, has 16 transmit or receive channels depending on the mode of operation for the array. The IQ signals are sampled at 245.76 MHz. In order to characterize the phase/gain corrections that need to be applied to obtain a calibrated signal, signal tones are collected from 0.001 to 1 GHz in 200 MHz subbands with a 1 MHz step size. The calibration method used implements a matched filter to calibrate the signals relative to a chosen reference channel. For a reference signal at reference tx channel m'_r , reference frequency n_r and reference rx channel m_r , the signal takes the form:

$$s_{m'_r, m_r, n_r}(k) = A_{m'_r, m_r, n_r} e^{j(2\pi f_{n_r} k + \phi_{m'_r, m_r, n_r})}. \quad (3.4)$$

The reference transmit channel is chosen by finding the channel with the weakest energy. The signal energy can be calculated as,

$$E = \int_{-\infty}^{+\infty} |s(t)|^2 dt, \quad (3.5)$$

or equivalently,

$$E = \sum_0^{K-1} |s(k)|^2. \quad (3.6)$$

The energy of the reference signal is,

$$E_r = \min(E(m', m, n)), \forall m', m, n. \quad (3.7)$$

With the energy of the reference signal, we can calculate the amplitude scaling required to match any signal with the reference signal

$$A = \sqrt{\frac{E_r}{E_{m', m, n}}}. \quad (3.8)$$

Following an approach similar to Mazurek and Rytel-Andrianik in [6], we use a matched filter approach to find the phase shifts between the channels in the array. This can be performed because we are assuming that the signals being transmitted or received by the array are the same for each channel. The result of the matched filtering of the signal from transmit channel m' , to receive channel m , at frequency n and the reference transmit-receive channel pair is

$$y(k) = \sum_{l=0}^{K-1} A_{m',m,n} e^{j(2\pi f_n l + \phi_{m',m,n})} A_{m',m_r,n} e^{j(2\pi f_n (k-l) + \phi_{m',m_r,n})}. \quad (3.9)$$

The matched filter will have a maximum at the point where the two signals overlap when $2\pi f_n l + \phi_{m',m,n} = 2\pi f_n (k-l) + \phi_{m',m_r,n}$. Calculating the angle at the maximum will result in the phase shift between the signal from transmit channel m' , receive channel m , and frequency n and the reference transmit-receive channel pair. The phase shift is calculated as:

$$\phi = \tan^{-1} \left(\frac{\Im(\max(y(k)))}{\Re(\max(y(k)))} \right). \quad (3.10)$$

The amplitude scalings and phase shifts from equations 3.8 and 3.10 are combined into a matrix of complex values with the form

$$C_{m',m,n} = A_{m',m,n} e^{-j\phi_{m',m,n}}. \quad (3.11)$$

The complex values are then applied to the corresponding signals to get the calibrated signals

$$S_{m',m,n} = C_{m',m,n} s_{m',m,n} \quad (3.12)$$

where S is the calibrated signal matrix, C is the matrix of calibration coefficients, and s is the uncalibrated signal matrix.

3.5 Analysis Methods

In order to test the temporal stability of the calibration coefficients, data will be collected over many days and the calibration coefficients calculated will be compared. Digital beamforming (DBF) will also be reviewed and applied to calibrated and uncalibrated signals to show the results of applying the calibration.

3.5.1 Temporal Analysis

For the temporal analysis, the standard deviation of the calibration coefficients is used. The standard deviation will indicate how closely the calibration follows the mean and will be shown for each channel and frequency. The mean calibration will be taken over multiple days and applied to the signals before transmit to verify the stability. Other calibration procedures did not investigate the temporal stability of their systems or calibration procedures so digital beamforming will be used as an additional measure to show the effectiveness of calibration.

3.5.2 Digital Beamforming Analysis

With antenna arrays there are many things that affect the response to an impinging plane wave. The position of the array elements, direction and frequency of the incoming signal, and hardware specifications of each array element have an effect on the beam pattern. There are many types of beamformers but for this research, a Discrete Fourier Transform (DFT) beamformer as described in [1] is used. For the vector of received signals $\mathbf{x}(n) = [x_0(n), x_1(n), \dots, x_{M-1}(n)]$, where M is the number of elements in the array, $\mathbf{X}\{m\}$ is the DFT in the m th frequency bin. Typically, each frequency bin is processed separately with a beamforming algorithm as

$$\mathbf{Y}\{m\} = \mathbf{w}^H\{m\}\mathbf{X}\{m\}, \quad (3.13)$$

where $\mathbf{Y}\{m\}$ is the result of beamforming and $\mathbf{w}^H\{m\}$ is the hermitian transpose of the vector of complex weightings applied to each channel. For an impinging wave with the unit direction vector \mathbf{a} , the wavenumber corresponding to the wave is $\mathbf{k} = -\frac{2\pi}{\lambda}\mathbf{a}$. The array manifold vector $\mathbf{v}_k(k)$ describes the spatial characteristics of the array and is defined as

$$\mathbf{v}_k(k) = \begin{bmatrix} e^{-j\mathbf{k}^T \mathbf{p}_0} \\ e^{-j\mathbf{k}^T \mathbf{p}_1} \\ \vdots \\ e^{-j\mathbf{k}^T \mathbf{p}_{M-1}} \end{bmatrix}, \quad (3.14)$$

where \mathbf{p} is a vector containing the position of array elements $0, \dots, M - 1$. The array manifold vector from Equation 3.14 is applied to the DFT result for a range of angles to give the resulting digital beam in Equation 3.13.

From the DBF result, values of interest can be extracted to show the performance of the array. The gain, first null depth, and first side lobe level are calculated and compared before and after calibration to the ideal case. Figure 3.3 shows the gain, first null depth, and first side lobe level for an example ideal,calibrated, and uncalibrated signal. In Figure 3.3, something to note is that due to the step size in angle, the values are not exact. An example of this is the value shown for the first null. Theoretically, the null would appear at $-\infty$ dB but due to the sampling in angle, it appears around -32 dB. The gain, first null depth, and first side lobe level are also shown for the signals calibrated before transmit with the mean calibration discussed in Section 3.5.1. The results of the beams formed using the calibration methods discussed in Section 2.1 are also shown in comparison to the proposed method.

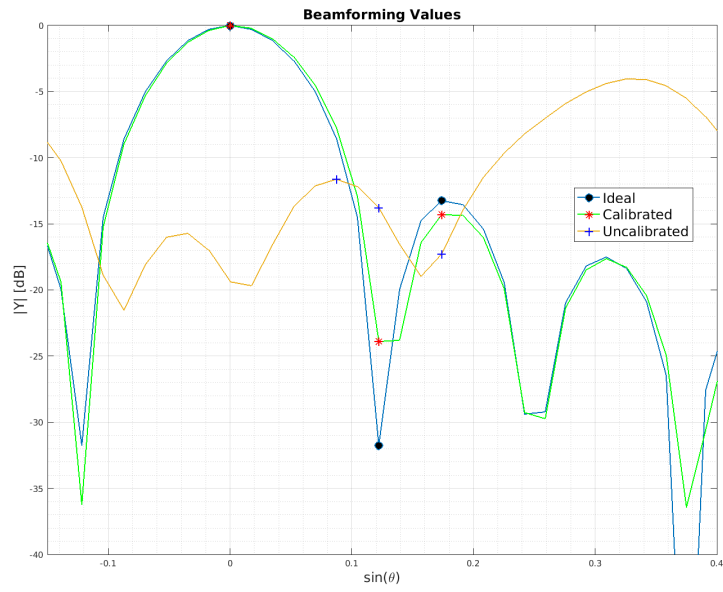


Figure 3.3: Example of calculated beamforming points for normalized ideal, calibrated, and uncalibrated digital beams

Results

4.1 Introduction

This section presents the results after applying the calibration algorithm proposed in Chapter 3 to measured data. Previous works provide little analysis on the calibration results [3,5]. The paper by Gaydos et al. show the results of calibration of an SDR array with a polar plot of the phase and amplitude of each channel in the array. In the paper by Campo et al., the results are shown with phase error between estimated direction of arrival and the real angle. However, the results in this chapter show the calculated phase and amplitude error and correction. The performance of the calibration algorithm is demonstrated by the restoration of the ideal main lobe and side lobe structure following digital beamforming. The phase and amplitude calibration performance are compared to results from the methods in [3,5].

4.2 Data

The variables used to characterize the performance of the system include channel, frequency, Rx/Tx gain values of the SDRs, and date of collection. Table 4.1 presents the data collections. Each set of data includes signals from each of the 16 channels and 9 center frequencies. As discussed in Section 3.4, the chirp data sets contain a single pulse per channel

Table 4.1: Dataset Characteristics

Dataset Name	Mode	Signal Type	Rx Gain	Tx Gain
2023Mar14	Tx	Chirp	30	20
2023Mar14 1	Tx	Chirp	30	20
2023Mar14 2	Tx	Chirp	30	20
2023Mar14 3	Tx	Chirp	30	20
2023Feb24	Rx	Chirp	30	20
2023Feb17	Rx	Chirp	30	20
2023Feb17 1	Rx	Chirp	30	20
2023Feb17 2	Rx	Chirp	30	20
2023Feb17	Tx	Chirp	30	20
2023Feb15	Rx	Chirp	30	20
2023Feb015 1	Rx	Chirp	30	20
2023Feb15 2	Rx	Chirp	30	20
2023Feb10	Rx	Chirp	30	20
2023Feb10 1	Rx	Chirp	30	20
2023Feb10 2	Rx	Chirp	30	20
2023Feb10 3	Rx	Chirp	30	20
2023Feb09	Rx	Chirp	30	20
2023Feb09 1	Rx	Chirp	30	20
2023Feb09	Tx	Chirp	30	20
2023Feb09	Rx	Chirp	27	17
2023Feb09	Tx	Chirp	27	17

for each center frequency and the tone data sets contain 200 pulses. As more data was collected, errors in the system setup became apparent. Data collected before Feb. 9th contains an SDR that was not synchronized with the others. The unsynchronized SDR resulted in 4 channels that would have different phase behavior as a function of frequency depending on the synchronization of the board. The synchronization error was fixed for the data collected after that date but for the results shown, data sets collected before Feb. 9th will be ignored.

Another thing to note about the data is a large spike in DC energy for the first frequency band. This results in a greater energy than the signals in other frequency bands. This could be removed using a high pass filter or other methods but since signals at lower frequencies are not of interest for this research, the signals are ignored. Figure 4.1 shows the frequency spectrum of the second frequency subband for the received chirp data collected on Feb. 24th. The figure shows the received chirp after digital down conversion,

centered at baseband. From Figure 4.1, we observe that the frequency of the transmitted signal has an effect on the magnitude of the received signal.

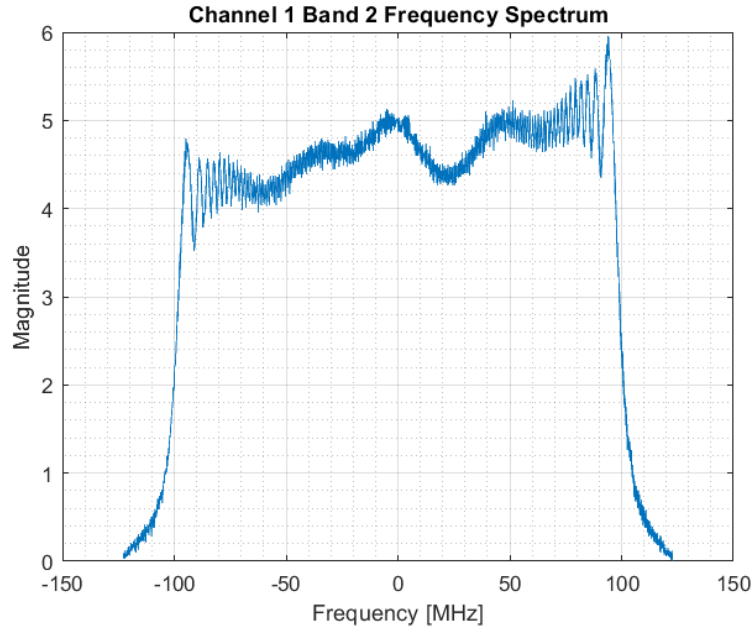


Figure 4.1: Example of frequency spectrum of channel 1 received chirp at center frequency 200 MHz

4.3 Phase and Amplitude Error

The calibration algorithm proposed in Section 3.4 focuses on the phase and amplitude correction applied to correct for the errors accumulated as the signals go through the system.

4.3.1 Phase Error

The phase error of the system is calculated in the same way that the phase correction is calculated. The error $\Delta\phi$ is calculated as $\Delta\phi = \phi_{actual} - \phi_{nominal}$, and the correction is $\phi_{corr} = -\Delta\phi$. For this case, ϕ_{actual} is the measured phase of the signal at a particular channel and frequency and $\phi_{nominal}$ is the measured reference phase. As an example, Figure

4.2 shows the phase error between the reference channel 5 and channel 1 versus center frequency for chirp signals in the receive mode. From Figure 4.2, we can see that the phase

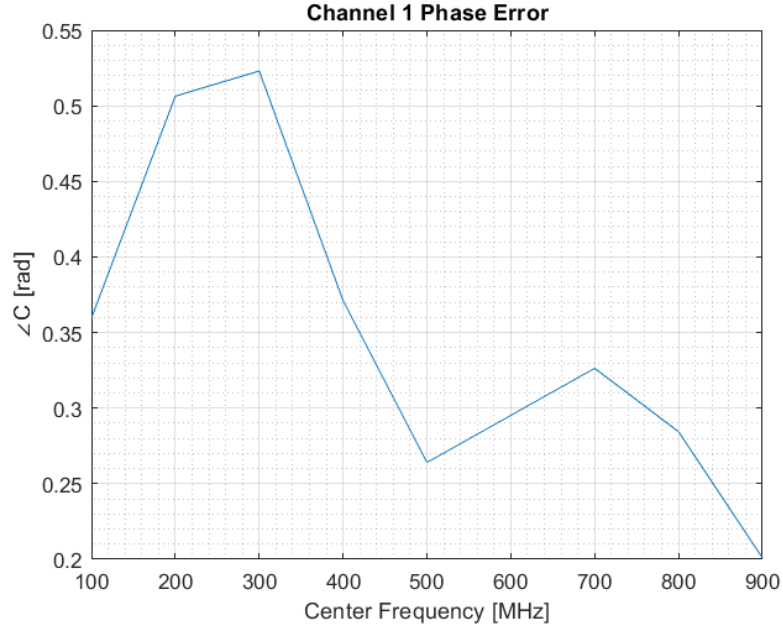


Figure 4.2: Channel 1 phase error vs frequency of Feb. 24th received chirp data

error for the first channel in the array is within 0.5 radians of channel 5 before calibration. In Section 4.4.1, the stability of the phase behavior of the system will be shown.

4.3.2 Amplitude Error

The amplitude error is calculated as $\Delta A = \sqrt{\frac{E_r}{E_{m',m,n}}}$, where $E_{m',m,n}$ is the energy of the signal for transmit channel m' , receive channel m , and frequency band n . As described in Section 3.4, the energy of each signal is scaled to the same level based on the lowest energy received. In Figure 4.3, the amplitude error is shown for the first receive channel of the Feb. 24th received chirp data set. From Figure 4.3, we can see the trend in energy as a function of frequency since the amplitude correction is inversely proportional to energy. For this data set, 600 MHz center frequency had the lowest energy and was chosen as the reference

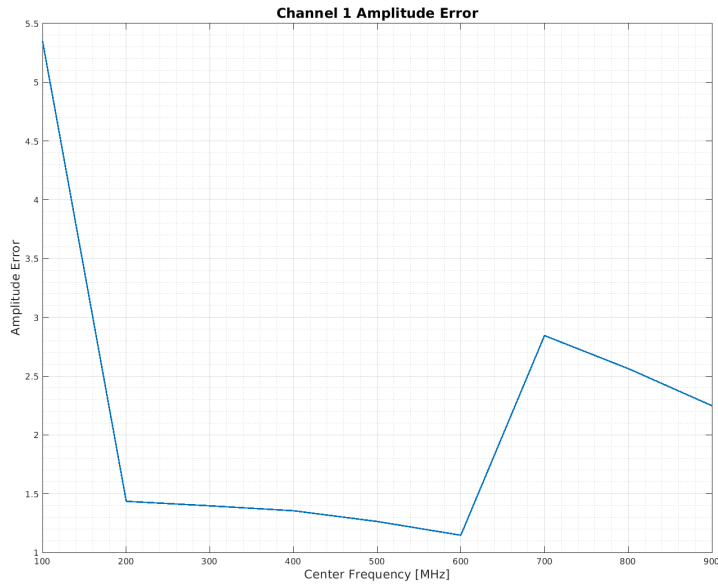


Figure 4.3: Channel 1 amplitude error vs frequency of Feb. 24th received chirp data

subband. Although the amplitude errors are random for each channel and frequency, the errors follow a general trend across data collections that will be shown in Section 4.4.2.

4.4 Phase and Amplitude Correction

If the phase and amplitude corrections required for a system do not vary much over time, it suggests that the system is stable. In order to determine the stability of the calibration coefficients and the system as a whole, data was collected over different days at different times. If the system shows to be stable, a set of previously calculated calibration coefficients can be reused to achieve similar results to performing a full calibration procedure.

4.4.1 Phase Correction

The phase correction for channel 1 of the Feb. 24th received chirp data is shown in Figure 4.4. The correction was calculated using the method in Section 3.4. To show the stability

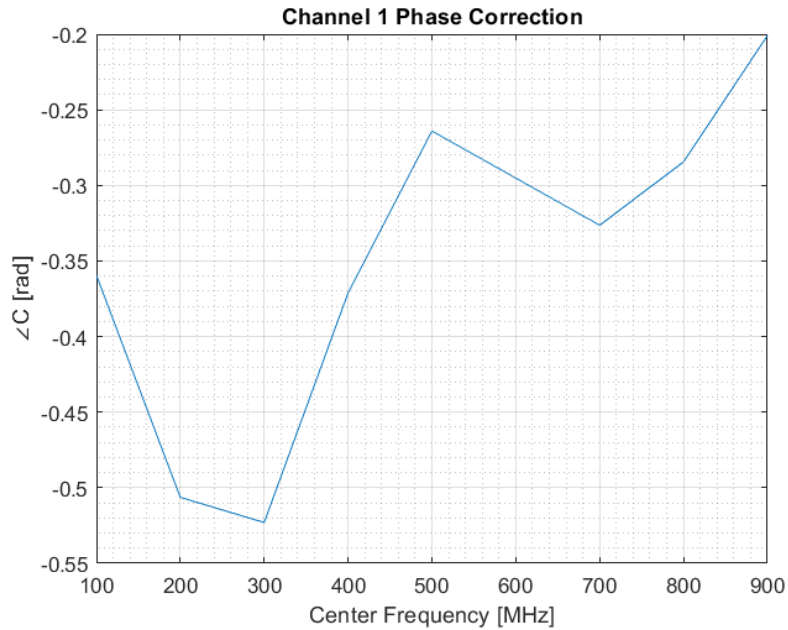


Figure 4.4: Phase correction of channel 1 vs frequency for Feb. 24th received chirp data

of the phase correction, the standard deviation of the phase correction is shown in Figure 4.5. The standard deviation was calculated for each center frequency and channel across the data collections from Feb. 10th, Feb. 17th, and Feb. 24th. From Figure 4.5, we can see that the standard deviation of phase is within 2 degrees for most channels in the array and within 8° in the most extreme case. As mentioned in Section 2.1, Schediwy et al. found that for a 16 element array, phase errors of 10° reduce the ability of the array to detect signals by less than 1% of the ideal capability of the array [9]. This suggests that the system is stable enough to not need recalibration over the course of a few weeks.

4.4.2 Amplitude Correction

The amplitude correction was calculated using the method described in Section 3.4 and plotted for the first channel versus center frequency of the pulses in Figure 4.6. To show the stability of the amplitude correction, the standard deviation is shown in Figure 4.7.

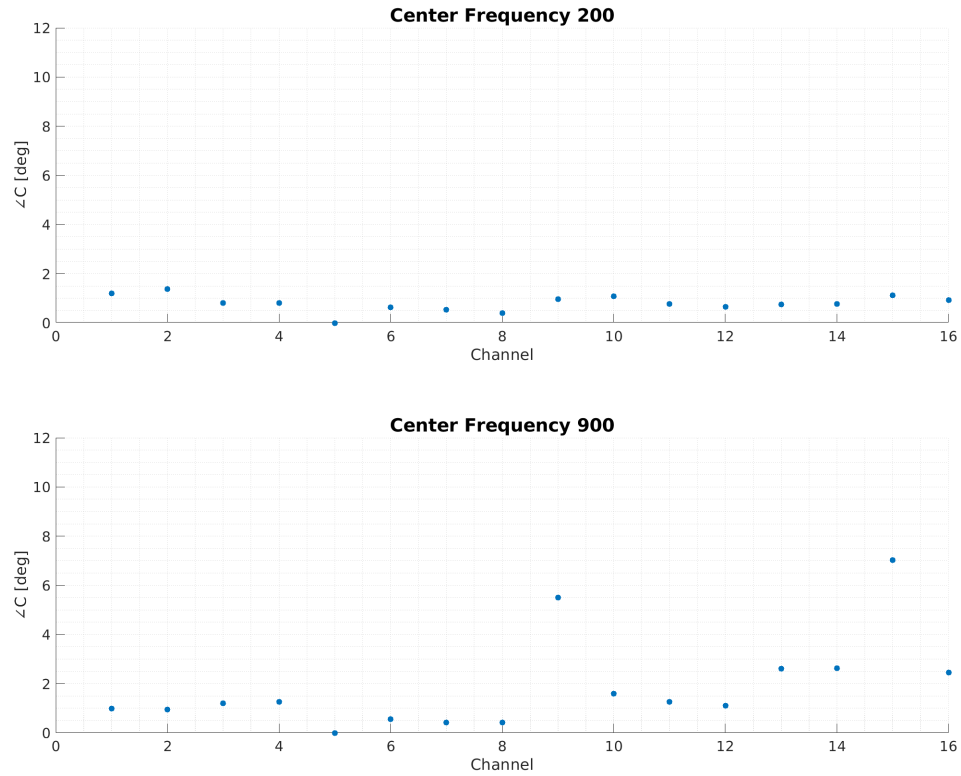


Figure 4.5: Standard deviation of phase correction vs channel for center frequencies 200 and 900 MHz

From Figure 4.7, we can see that the standard deviation of amplitude correction values for all channels is less than 0.06. This suggests that regardless of date or time of data collection, the amplitude of received signals is stable. In order to quantify the effect the variation in phase and amplitude has on the calibration, beamforming is applied to the signals.

4.5 Effects on Beam Quality

Beamforming is applied to the uncalibrated and calibrated signals to show how the calibration affects the beam shape. To show the effectiveness of calibration, main beam gain, first side lobe level, and first null depth are extracted from calibrated and uncalibrated beams.

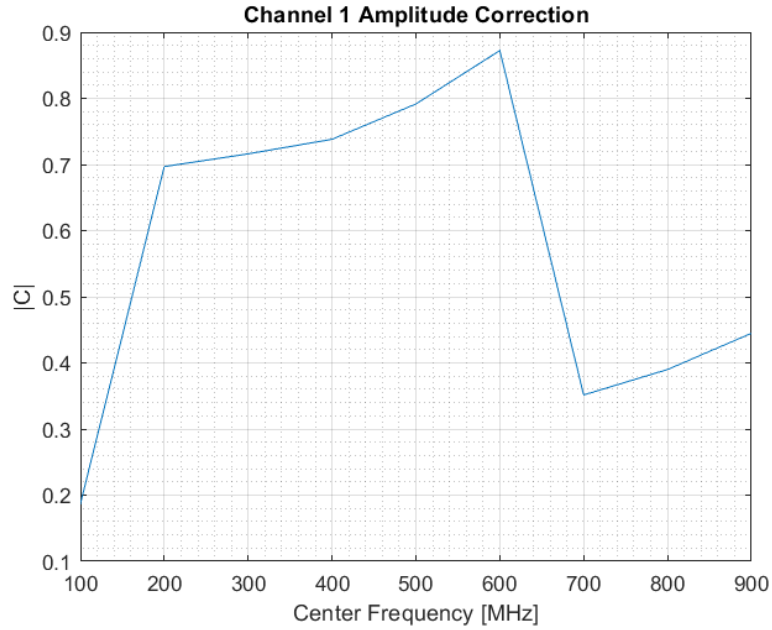


Figure 4.6: Amplitude correction of channel 1 vs frequency for Feb. 24th received chirp data

In the Figures 4.8, 4.9, and 4.12, a mean calibration was calculated over the received chirp datasets from Feb. 10th and 17th. A sample case from Feb. 10th with calibration calculated from the proposed method is shown along with the same data calibrated with the mean calibration coefficients. Data collected a week later on Feb. 24th and on Mar. 14th were also shown after calibration with the same mean calibration values.

4.5.1 Gain

The main beam gain is shown in Figure 4.8. It was calculated by finding the maximum value within the half-power beamwidth (HPBW). In u space, the HPBW can be calculated as $1.782\frac{1}{N}$ [1], where N is the number of elements in the array. In Figure 4.8, the gain for the calibrated and uncalibrated beams are shown in dB with respect to center frequency. The figure shows an increase in gain with the calibrated data but it also shows that whether the mean calibration is used or the full calibration procedure, the results are similar. It also

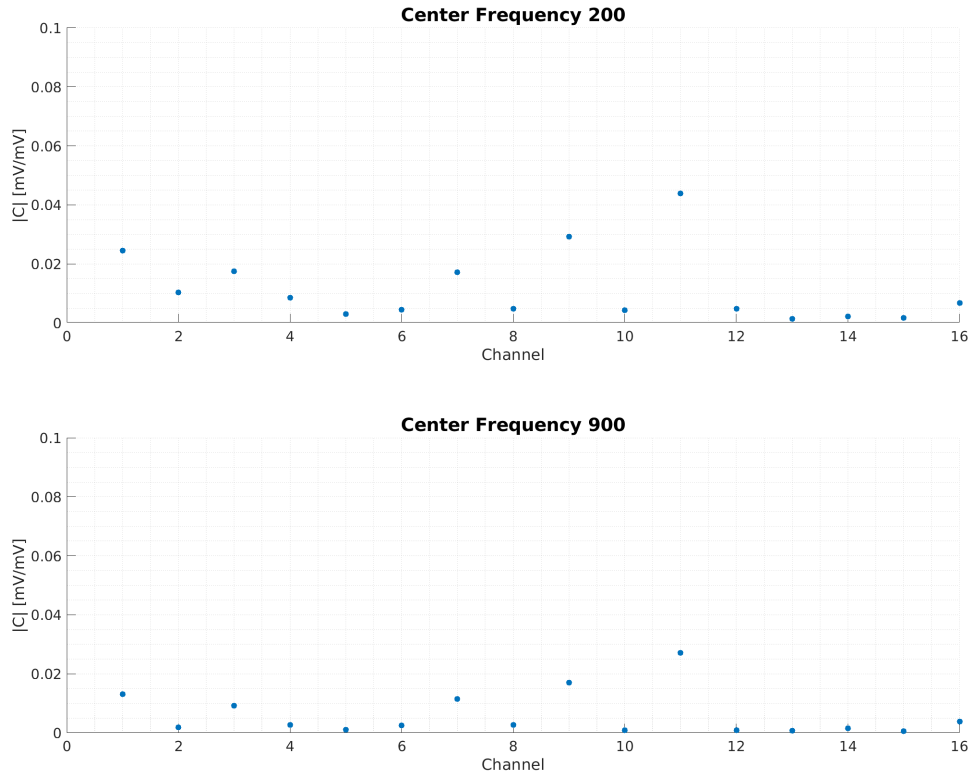


Figure 4.7: Standard deviation of the amplitude correction vs channel for center frequencies 200 and 900 MHz

shows the stability of the system and the calibration. Even though the mean calibration was calculated a month before, the Mar. 14th data set shows the same trend as the Feb. 10th data after calibration.

4.5.2 First Side Lobe Level

The first side lobe level is also a good measure of a calibration method's performance. To find the level of the first side lobe, the location in u space was calculated with the equation [1]

$$u = \pm \frac{2m + 1}{N} \frac{\lambda}{2d}, m = 1, 2, \dots \quad (4.1)$$

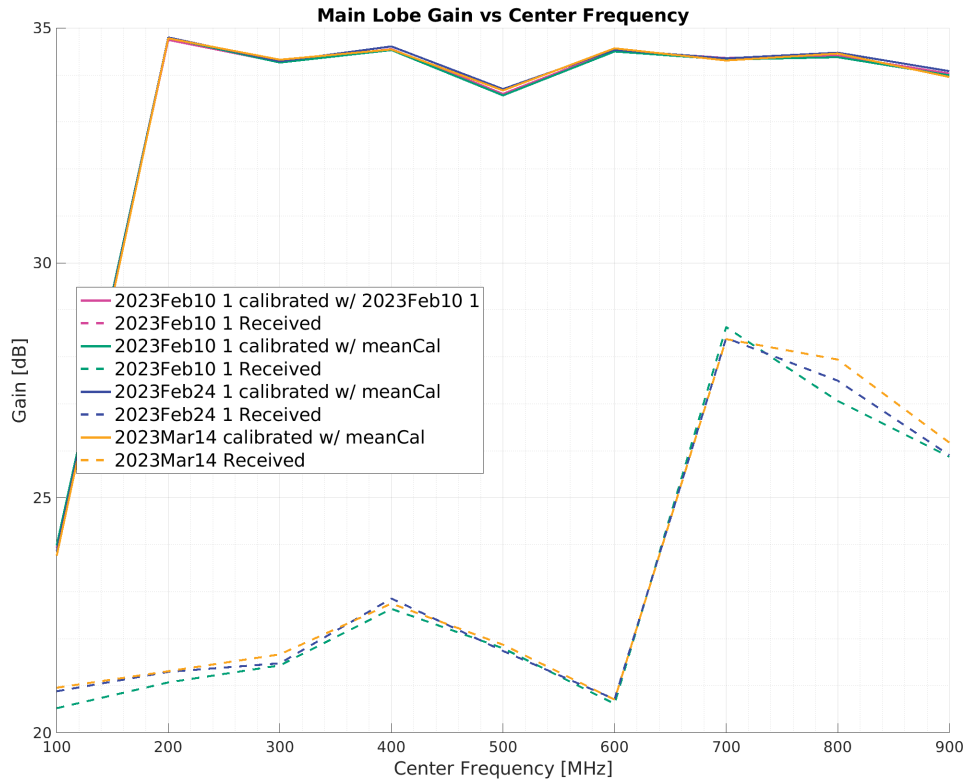


Figure 4.8: Main lobe gain with different calibrations applied

where N is the number of elements in the array, λ is the wavelength, d is the physical spacing of the array elements, and m is the side lobe number. Since there is no physical array, we allow d to be $\frac{\lambda}{2}$. This simplifies the equation to give us $u = \frac{3}{N}$ or 0.1875 in u space for this array. The side lobe level is shown in dB with respect to center frequency. Figure 4.9 shows the side lobe level of the calibrated and uncalibrated signals versus center frequency. From Figure 4.9, we can see that the calibration procedure brings the side lobe level within 1 dB of the ideal value. The calibrated Mar. 14th data suggests that the mean calibration can be used as long as the system is stable enough. The variation in phase and gain over time does not have a significant effect on the peak sidelobe level after digital beamforming. If we instead look at the first side lobe level at a particular center frequency, we can better visualize the effect of calibration. Figure 4.10 shows the side lobe level

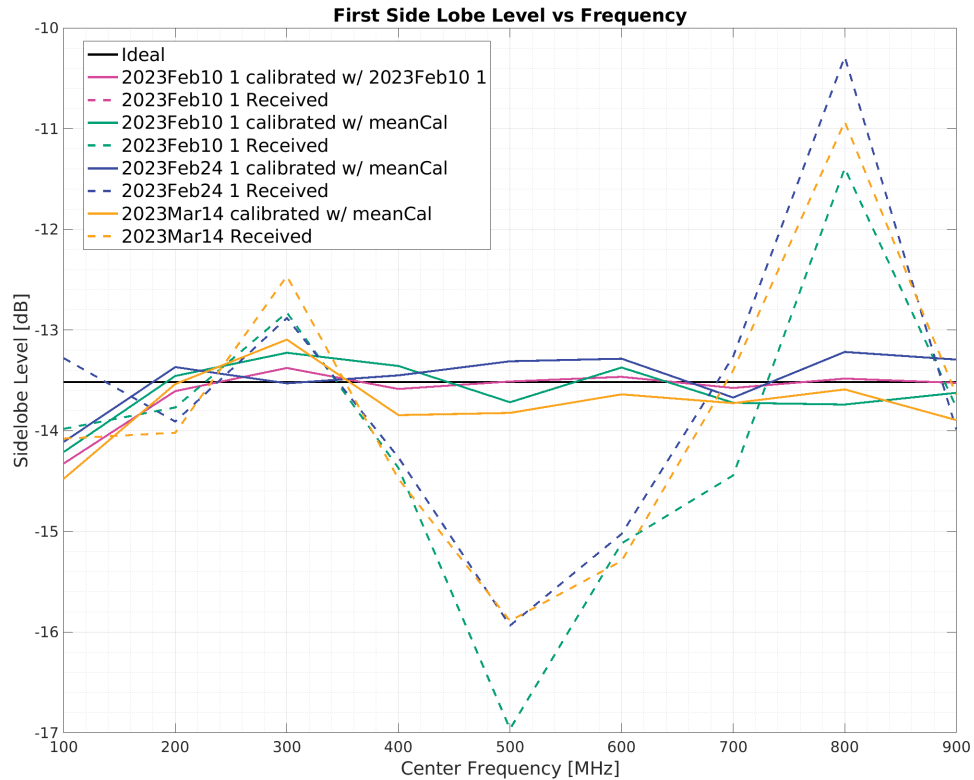


Figure 4.9: First side lobe level with different calibrations applied

at center frequency 200 MHz for the same data shown in Figure 4.9. We can see that the calibrated side lobe levels are closer to the ideal. The lower side lobe levels of the uncalibrated case are an artifact of the steering of the uncalibrated array. The theoretical side lobe location does not match where the actual location is. Figure 4.11 demonstrates the lower side lobe locations. The uncalibrated beam is shown as the “Received” line on the legend. Figure 4.11 also shows that the calibrated and ideal beams have good agreement.

4.5.3 First Null

Another statistic of interest to show the effectiveness of calibration is the depth of the first null. The null should have a value of $-\infty$ for the ideal case but it is shown at -32 dB in Figure 4.12. This is due to the sampling in angle during beamforming. The first null

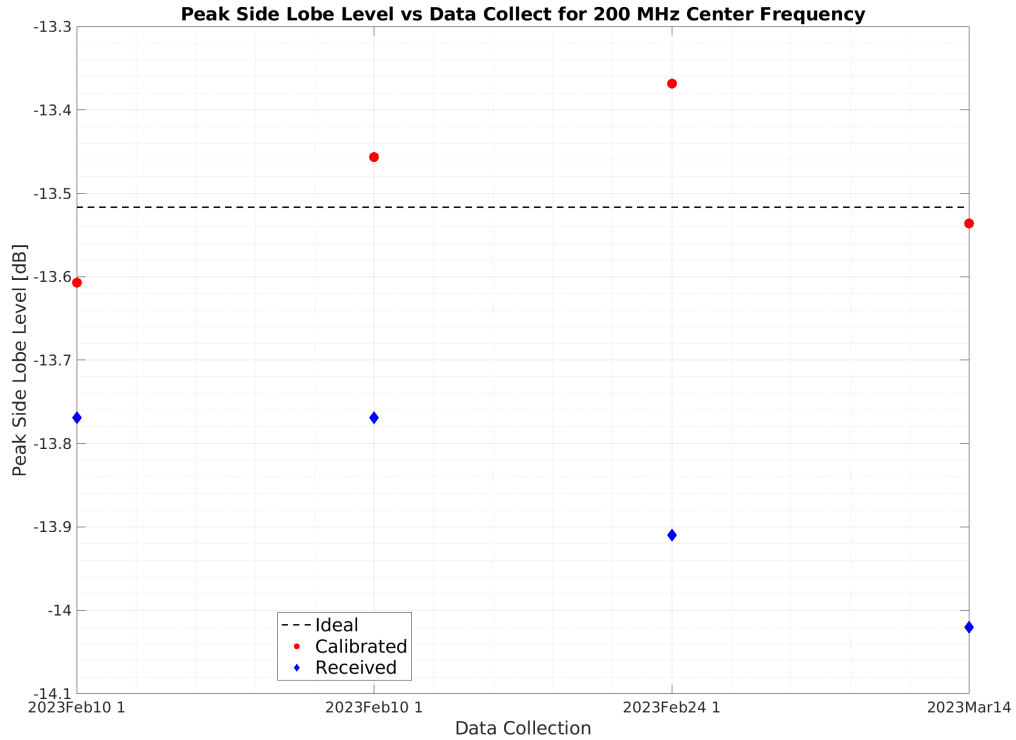


Figure 4.10: Calibrated and uncalibrated first side lobe level vs data collect for 200 MHz center frequency

occurs at $\frac{\lambda}{Nd}$ in u space [1], where λ is the wavelength, N is the number of channels in the array, and d is the distance between physical elements. Since there isn't a physical array, d was set to $\frac{\lambda}{2}$. This resulted in the first null being located at $\frac{2}{N}$ or 0.125 in u space for this particular array. The null depth is shown in dB with respect to center frequency. From Figure 4.12, we see that for the center frequencies of interest, 200, 300, ..., 900 MHz, the depth of the first null is at least -28 dB for calibrated sets of data. Figure 4.13 shows the depth of the first null versus data collect for 200 MHz center frequency before and after calibration.

4.6 Calibration on Transmit

The previous Figures helped demonstrate the stability of the system in the Rx mode. If the user of this system wanted to transmit signals, a calibration is required before transmitting the signals. Using the system configuration described in Section 3.1 for the Tx mode, calibration coefficients were found for transmitted chirps and applied before transmitting. Figures 4.14 and 4.15 show the standard deviation of the phase and amplitude corrections of each channel for the 200-MHz and 900-MHz center frequencies. The data included came from the Feb. 17th and Mar. 14th data collections. From the figures we can see that the calibration values on transmit are consistent in both amplitude and phase for each of the channels. For the transmit data, there are only 2 data sets that were collected after Feb. 8th since the main focus was on the receive side. Given that there were only 2 data sets, the mean calibration was calculated with the Feb. 9th and 17th data collections. This mean calibration was applied on Mar 14th to 3 sets of data. Figures 4.16 to 4.18 show the main lobe gain, null depth, and peak side lobe level versus frequency for the signals calibrated on transmit as the “Received” signals in the dashed lines. The calibrated signals were calibrated again using the same procedure and the results are also shown on the figures as the solid lines. The figures show that reapplying the calibration does not improve the gain, null depth, and side lobe level a noticeable amount. The received signals that were calibrated on transmit and the recalibrated signals were shown using digital beamforming compared to the ideal beam shape for the 200 MHz and 900 Mhz cases in Figure 4.19. From Figure 4.19 we can see that the calibration applied on transmit shown as the “Received” line on the graphs shows very good agreement to the ideal beam shape.

The presented method described in Section 3.4 is also compared to the methods reviewed in Section 2.1. Tables 4.2, 4.3, and 4.4 show the calculated gain, peak side lobe

Gain			
Frequency	MMAC	Campo	Gaydos
100 MHz	51.7729	44.1544	14.9574
200 MHz	61.7936	54.1874	81.3907
300 MHz	61.7875	54.1813	80.9796
400 MHz	61.7907	54.1844	81.1051
500 MHz	61.7888	54.1826	79.7206
600 MHz	61.7928	54.1865	81.3313
700 MHz	61.7909	54.1847	79.6423
800 MHz	61.7911	54.1848	80.0817
900 MHz	61.7895	54.1832	81.9710

Table 4.2: Calculated Gain Values of Rx Tone Data from March 14th Data Collection Calibrated with Different Methods

Side Lobe Level			
Frequency	MMAC	Campo	Gaydos
100 MHz	-13.7804	-14.7091	-19.0646
200 MHz	-13.5163	-13.5160	-12.7388
300 MHz	-13.5071	-13.5116	-13.0250
400 MHz	-13.5135	-13.5136	-12.3518
500 MHz	-13.5154	-13.5147	-13.8872
600 MHz	-13.5172	-13.5165	-11.7854
700 MHz	-13.5160	-13.5154	-18.8469
800 MHz	-13.5167	-13.5165	-13.2269
900 MHz	-13.5164	-13.5158	-12.3730

Table 4.3: Calculated Peak Side Lobe Values of Rx Tone Data from March 14th Data Collection Calibrated with Different Methods

level, and first null depth for each calibration method respectively. The tables suggest that the proposed calibration method and method proposed by Campo et al. in Section 2.1.2 perform similarly. The calibration method proposed by Gaydos et al. in Section 2.1.3 did not perform as well for this system. Although the gain was higher, the side lobe level and null depth is inconsistent and deviates from the ideal. This could be due to the number of samples received for each pulse. The calibration technique in Section 2.1.3 was intended

Null Depth			
Frequency	MMAC	Campo	Gaydos
100 MHz	-29.1489	-24.6466	-14.2797
200 MHz	-31.7634	-31.7634	-13.7829
300 MHz	-31.8429	-31.8007	-20.6986
400 MHz	-31.7872	-31.7821	-23.2542
500 MHz	-31.7872	-31.7894	-25.9006
600 MHz	-31.7590	-31.7610	-16.4505
700 MHz	-31.7622	-31.7650	-24.0226
800 MHz	-31.7572	-31.7589	-26.1511
900 MHz	-31.7762	-31.7788	-14.2980

Table 4.4: Calculated Null Depth Values of Rx Tone Data from March 14th Data Collection Calibrated with Different Methods

to be used in a CW system. If there was an insufficient number of samples per pulse, the calculated correction values could be less effective. Figure 4.20 shows the calibrated digital beams from the methods presented in Section 2.1. The proposed method and method by Campo et al. show good agreement to the ideal case whereas the method proposed by Gaydos et al. does not. The method proposed by Gaydos et al. shows higher side lobe levels and null depths compared to the other two methods shown. Although the gain was higher for the method proposed by Gaydos et al. according to Table 4.2, the normalized beam shape shows less agreement with the ideal in side lobe level and first null depth as the proposed method described in Section 3.4 or method by Campo et al.

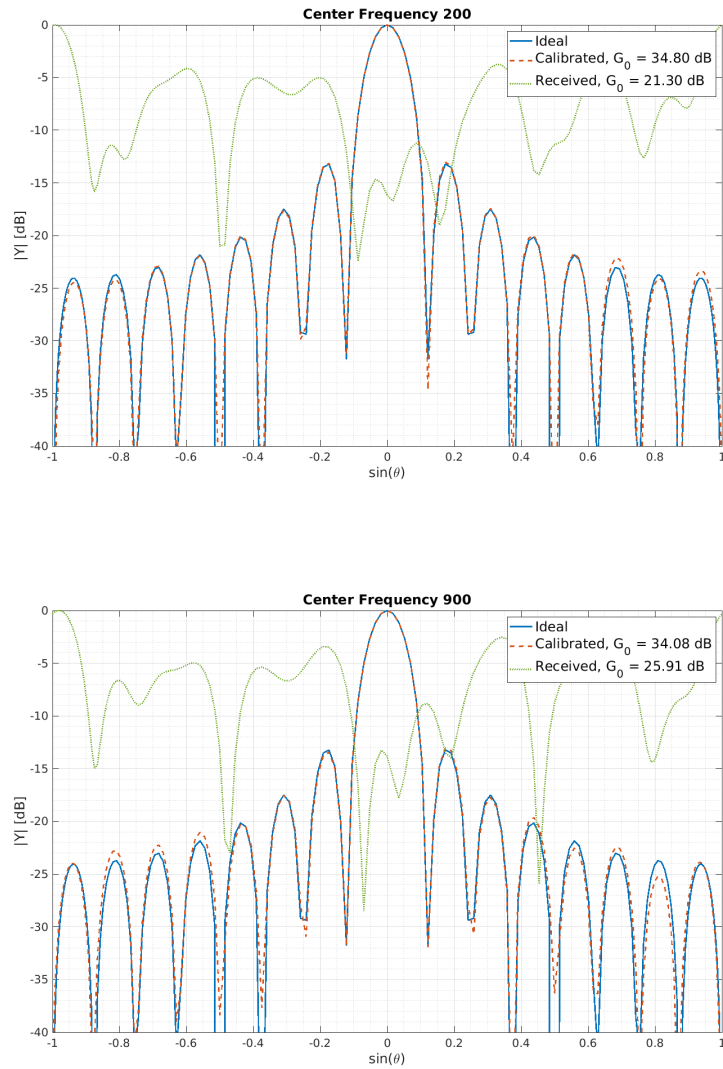


Figure 4.11: Beamforming results of Feb. 24th data with mean calibration applied for center frequencies 200 and 900 MHz

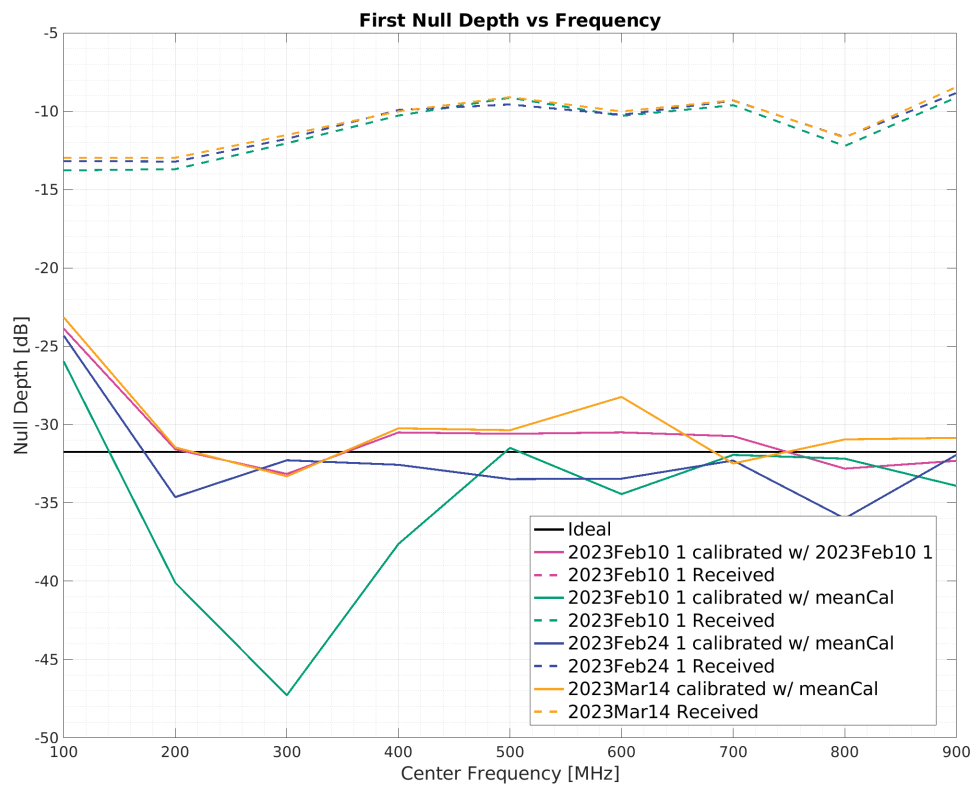


Figure 4.12: First null depth with different calibrations applied

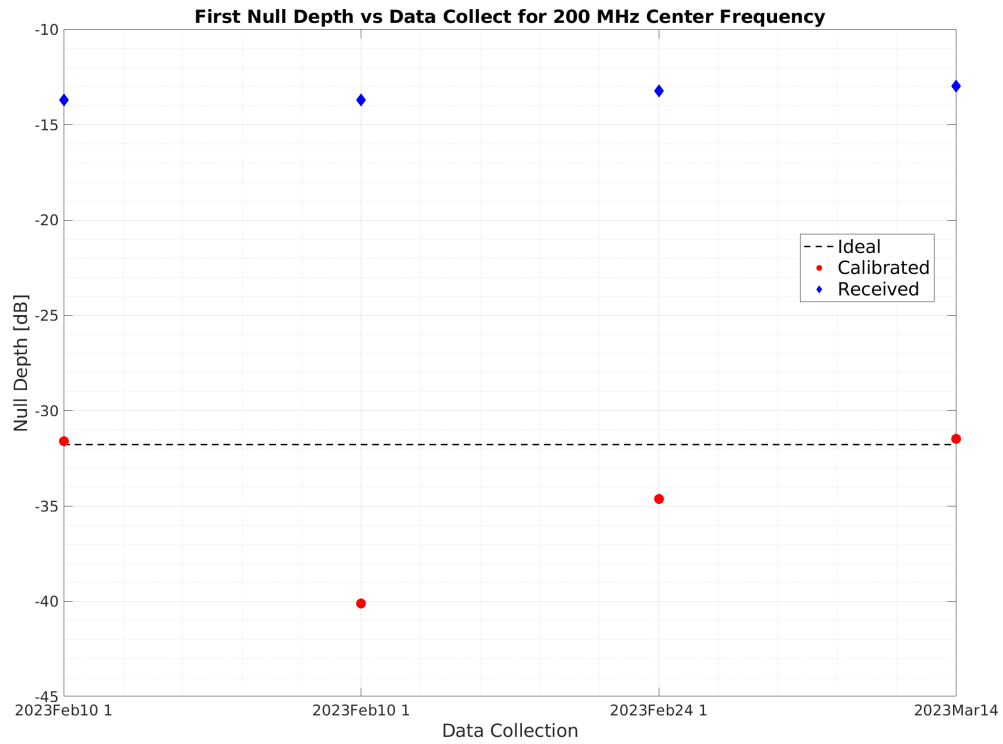


Figure 4.13: Calibrated and uncalibrated first null depth vs data collect for 200 MHz center frequency

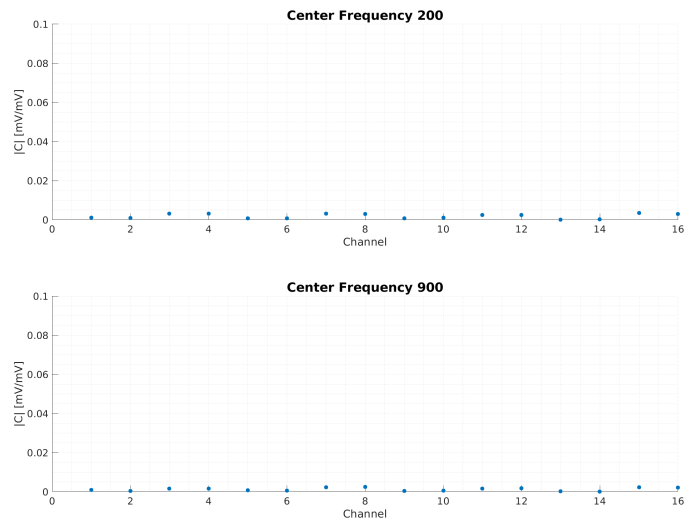


Figure 4.14: Standard deviation of amplitude correction for transmitted chirp signals at 200 and 900 MHz center frequencies

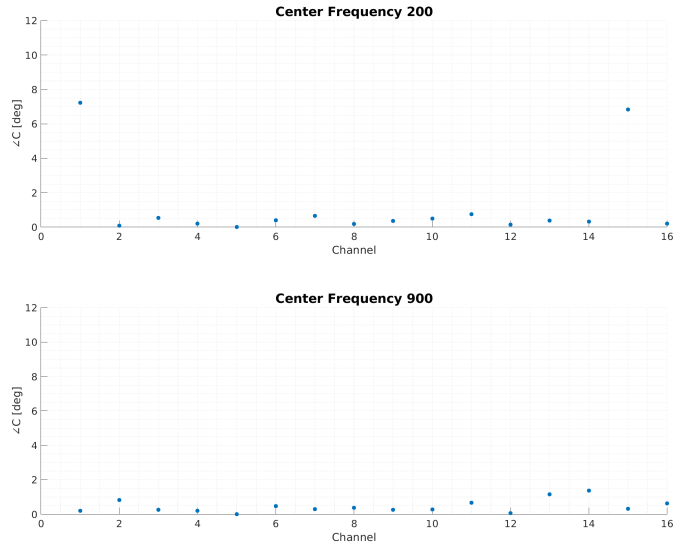


Figure 4.15: Standard deviation of phase correction for transmitted chirp signals at 200 and 900 MHz center frequencies

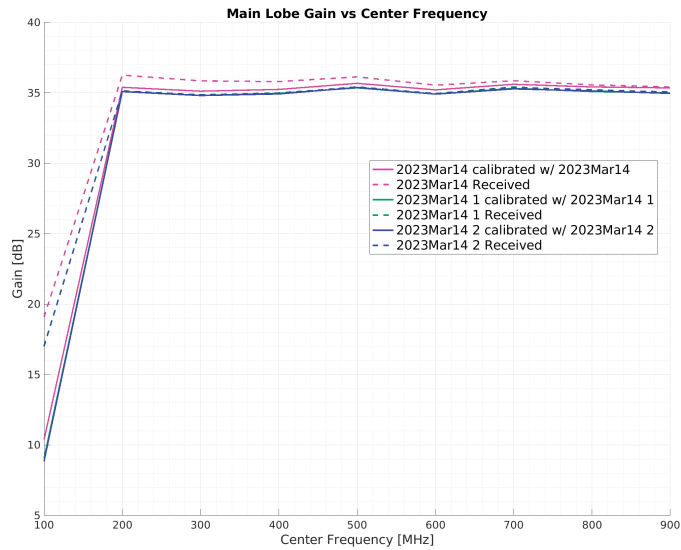


Figure 4.16: Main lobe gain for Mar. 14th data collection calibrated before transmit and recalibrated after receiving

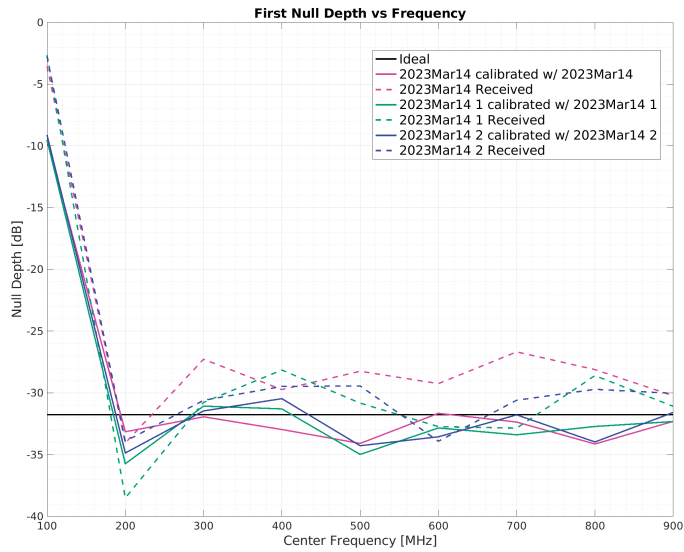


Figure 4.17: First null depth for Mar. 14th data collection calibrated before transmit and recalibrated after receiving

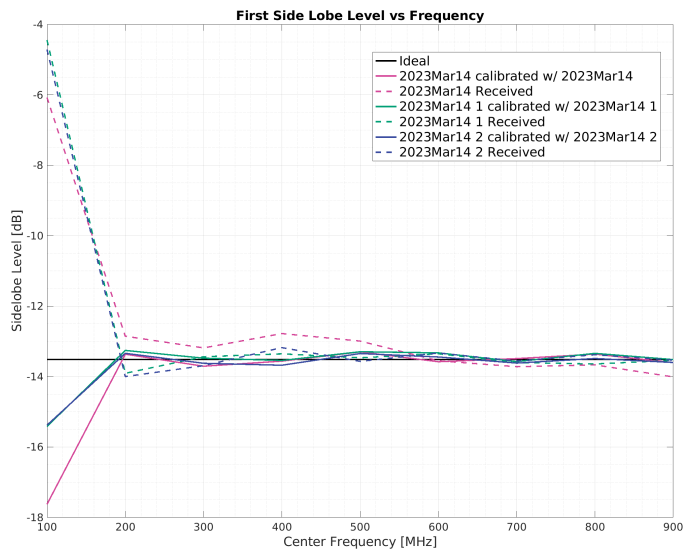


Figure 4.18: Peak side lobe level for Mar. 14th data collection calibrated before transmit and recalibrated after receiving

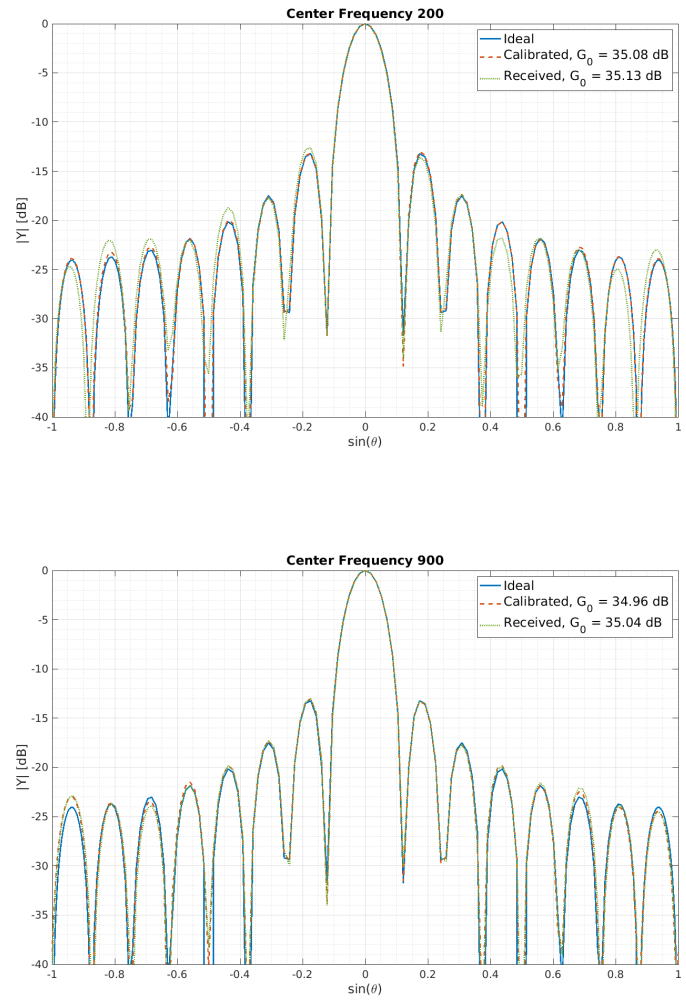


Figure 4.19: Beamforming results for Mar. 14th data collection calibrated before transmit and recalibrated after receiving

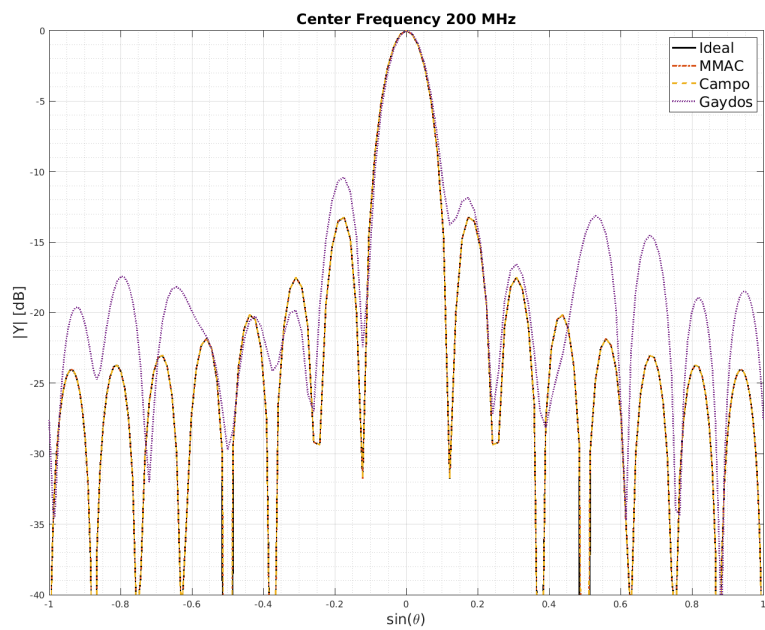


Figure 4.20: Calibrated Digital Beams for 200 MHz Rx Tone with Different Calibration Methods

Conclusion

This work introduced a matched filter approach to calibrate the phase and amplitude errors in a SDR array system. The stability of the system was shown through the standard deviation of phase and amplitude calibration correction factors over the course of a month. The performance of the calibration method was evaluated with the gain, peak side lobe level, and first null depth calculated after applying digital beamforming to the calibrated and uncalibrated signals.

Data was collected over the course of three weeks to show the stability of the calibration. Over the course of the three weeks, the standard deviation of the phase and amplitude correction were calculated. The phase correction showed a maximum standard deviation of 8° with most of the channels below 2° . The standard deviation of the amplitude correction was below 0.06 for all channels. The standard deviation of the phase and amplitude correction over the course of the three weeks suggest that the calibration coefficients are stable enough to be applied up to three weeks later. Due to time constraints, the limit to how long calibration values can be used for the given system was not found. Further research into how temperature and outside conditions affect the variance in the calibration coefficients would help to better understand how often calibration needs to be performed for the given system.

With a calibrated set of signals, digital beamforming was applied to evaluate the performance of the proposed calibration method. The gain, peak side lobe level, and first null depth of the proposed calibration method showed good agreement to the ideal case

with a difference of 0.2246 dB for the peak side lobe level and 0.3998 dB for the first null depth. The agreement of calibrated beam shape to the ideal suggests that the matched filter calibration method is sufficient for calibrating narrowband signals like tones or wideband signals like chirps. A course of additional research in this topic would be to include more variables such as gain and to account for mutual coupling between array elements. With the addition of mutual coupling, the calibration method would need to be adapted to decouple the signals.

Bibliography

- [1] H. L. Van Trees, *Arrays and Spatial Filters*. John Wiley & Sons, Ltd, 2002, ch. 2, pp. 17–89. [Online]. Available: <https://onlinelibrary.wiley.com/doi/abs/10.1002/0471221104.ch2>
- [2] E. Jones, “Software defined radios, cognitive radio and the software communications architecture (sca) in relation to comms, radar and esm,” in *2008 IET Seminar on Cognitive Radio and Software Defined Radios: Technologies and Techniques*, Sep. 2008, pp. 1–7.
- [3] D. Gaydos, P. Nayeri, and R. Haupt, “Calibration and synchronization of software-defined-radio arrays,” in *2020 IEEE International Symposium on Antennas and Propagation and North American Radio Science Meeting*, July 2020, pp. 2075–2076.
- [4] S. Henault and Y. Antar, “Wideband analysis of mutual coupling compensation methods,” *International Journal of Antennas and Propagation*, vol. 2011, 01 2011.
- [5] C. Campo, M. Stefer, L. Bernard, S. Hengy, H. Boeglen, and J. M. Paillot, “Antenna weighting system for a uniform linear array based on software defined radio,” in *2017 Mediterranean Microwave Symposium (MMS)*, Nov 2017, pp. 1–4.

- [6] G. Mazurek and R. Rytel-Andrianik, "Pilot-based calibration of dual-tuner sdr receivers," in *2020 28th European Signal Processing Conference (EUSIPCO)*, Jan 2021, pp. 1971–1975.
- [7] J. Mitola, "Software radios: Survey, critical evaluation and future directions," *IEEE Aerospace and Electronic Systems Magazine*, vol. 8, no. 4, pp. 25–36, April 1993.
- [8] C. Xiaoming, Z. Shuai, and L. Qinlong, "A review of mutual coupling in mimo systems." *IEEE Access*, vol. 6, pp. 24 706 – 24 719, 2018. [Online]. Available: <http://ezproxy.libraries.wright.edu/login?url=https://search.ebscohost.com/login.aspx?direct=true&db=edsdoj&AN=edsdoj.52a292c9d4f8410b94054a22e0217508&site=eds-live>
- [9] S. W. Schediwy, D. Price, F. Dulwich, and B. Mort, "A quantitative analysis of how phase errors affect the beam quality of phased arrays," in *2010 IEEE International Symposium on Phased Array Systems and Technology*, 2010, pp. 256–260.
- [10] *RSPduo General Specifications*, SDRplay. [Online]. Available: <https://www.sdrplay.com/wp-content/uploads/2018/06/RSPDuo-Technical-Information-R1P1.pdf>
- [11] Z. X. Sun, J. Q. Wang, and G. L. Wang, "Sensitivity analysis of the feed system for the tm vgos telescope," in *2020 12th International Conference on Communication Software and Networks (ICCSN)*, 2020, pp. 314–317.
- [12] S. Huber, M. Younis, G. Krieger, and A. Moreira, "Error analysis for digital beam-forming synthetic aperture radars: A comparison of phased array and array-fed reflector systems," *IEEE Transactions on Geoscience and Remote Sensing*, vol. 59, no. 8, pp. 6314–6322, Aug 2021.
- [13] Y. Xiao and Y. Wang, "Deep learning-based mutual coupling modeling and baseband decoupling algorithm for mimo systems," *IEEE Communications Letters*, vol. 24, no. 9, pp. 1986–1990, Sep. 2020.

- [14] *GNU Radio Software*, GNU Radio. [Online]. Available: <https://www.gnuradio.org/>
- [15] *OctoClock Spec Sheet*, Ettus Research, 4600 Patrick Henry Drive Santa Clara, CA 95054. [Online]. Available: <https://www.ettus.com/all-products/OctoClock/>
- [16] I. A. H. Adam and M. R. Islam, “Performance study of direction of arrival (doa) estimation algorithms for linear array antenna,” in *2009 International Conference on Signal Processing Systems*, 2009, pp. 268–271.
- [17] H. Nguyen-Le and T. Le-Ngoc, “Pilot-aided joint cfo and doubly-selective channel estimation for ofdm transmissions,” *IEEE Transactions on Broadcasting*, vol. 56, no. 4, pp. 514–522, 2010.
- [18] S. Samanta and T. V. Sridha, “Modified slow fading channel estimation technique and fast fading channel estimation technique for ofdm systems,” in *2018 3rd IEEE International Conference on Recent Trends in Electronics, Information & Communication Technology (RTEICT)*, 2018, pp. 1638–1643.
- [19] J. Amadid, A. Khabba, L. Wakrim, Z. E. Ouadi, and A. Zeroual, “An efficient hybrid pilot design for channel estimation in massive mimo systems,” in *2022 IEEE 2nd International Maghreb Meeting of the Conference on Sciences and Techniques of Automatic Control and Computer Engineering (MI-STA)*, 2022, pp. 447–451.